Nigerian Journal of Applied Physics (NJAP)
ISSN Print: 3115-5871
ISSN Online: 3115-588X
DOI: https://doi.org/10.62292/njap-v2i4-2026-107
Volume 2(4), December 2026

Numerical Analysis of Topological Phase Transitions in the Haldane Model: Berry Curvature, Chern Numbers, and Edge States

Iyanuoluwa Olaniyi Ajayi and Samuel Oyindamola Adeosun

[1]Department of Physics, Bamidele Olumilua University of Education, Science and Technology, Ikere Ekiti, Ekiti State, Nigeria.
[2]Department of Physics, Nigerian Defence Academy, Kaduna, Kaduna State, Nigeria.

*Corresponding author's email: ajayi.iyanuoluwa@bouesti.edu.ng Phone No.: 07031463948
ORCID iD : https://orcid.org/0009-0008-6399-0167

ABSTRACT

This study presents a numerical analysis of the topological phase transition in the minimal Haldane model using Berry curvature, Chern-number quantization, bulk-gap evolution, phase-boundary localization, and a finite-ribbon test of bulk-edge correspondence. The honeycomb-lattice Bloch Hamiltonian was evaluated with nearest-neighbour hopping $t_1=1$, next-nearest-neighbour hopping $t_2=0.1$, and a representative phase $\varphi=\pi/2$. The occupied-band Chern number was computed on a 122×122 Brillouin-zone mesh with the gauge-invariant Fukui-Hatsugai-Suzuki (FHS) method and cross-checked against a finite-difference Berry-curvature integral and a mesh-refinement test. For $M=-0.3$, 0.3, and 0.7, the calculated Chern numbers were −1, −1, and 0, respectively, with finite bulk gaps away from the transition, and the finite-difference curvature integral approached these quantized values as the mesh was refined. The critical masses, resolved on a scan step of 0.01 as $M\approx-0.52$ and $M\approx0.52$, agree with the analytical Haldane values $\pm3\sqrt{3}t_2\sin\varphi=\pm0.519615$ to within the scan resolution (relative discrepancy 0.074%), and bisection on finer meshes converges toward the analytical values. Direct evaluation at the two inequivalent Dirac points confirmed the expected gap closures. A zigzag ribbon of 40 unit cells was then used to test bulk-edge correspondence. Edge-resolved ribbon spectra show one chiral branch on each edge crossing the common projected bulk gap with opposite velocities in the topological phase, and no state inside the gap in the trivial phase. Edge-localized states inside the common projected gap number 202 for $M=0.3$ and none for $M=0.7$, and the counts change once the window extends beyond the gap, so they are used as supporting evidence only. The results are a numerical cross-validation of the established Haldane transition and not the discovery of a new phase.

Keywords: Haldane model, Chern insulator, Berry curvature, Chern number, Topological Phase Transition.

INTRODUCTION

The classification of quantum phases of matter has traditionally been based on local order parameters associated with spontaneous symmetry breaking. This method does not fully describe quantum phases whose defining properties arise from the global geometry and topology of electronic wave functions in momentum space. In topological band systems, an insulating bulk can possess conducting boundary states whose existence is determined by a global topological invariant rather than by conventional local order. The geometric phase acquired by a quantum state during adiabatic evolution provides the foundation for this description, while the Berry connection and Berry curvature provide the corresponding momentum-space geometric quantities (Berry, 1984; Xiao et al., 2010). In two-dimensional insulating systems, the integral of the Berry curvature over the Brillouin zone gives an integer-valued Chern number. This invariant is unchanged under continuous variations of the Hamiltonian as long as the bulk energy gap remains open and is directly related to the quantization of Hall conductivity (Thouless et al., 1982). The Haldane model gives one of the simplest theoretical realizations of a Chern insulator. It was introduced by Haldane (1988) and it describes spinless particles on a honeycomb lattice with real nearest-neighbor hopping, complex next-nearest-neighbor hopping, and a staggered sublattice potential. Its importance arises from the demonstration that a quantized Hall response can occur without a uniform external magnetic field. The complex

next-nearest-neighbor hopping breaks time-reversal symmetry while maintaining zero net magnetic flux through the unit cell, allowing non-trivial topology to emerge from the structure of the Bloch Hamiltonian itself (Haldane, 1988). The model has since proven theoretically important in the investigation of Chern insulating phases, quantum anomalous Hall physics, and topological phase transitions. Recent studies have continued to develop and extend the Haldane framework in order to understand Chern insulating phases, topological phase transitions, and the relationship between bulk topology and boundary states. Nadeem et al. (2020) provided a perspective review of the quantum anomalous Hall Effect and its relationship to the broader class of Chern-insulating systems. Their discussion begins with the Haldane model as the prototypical spinless Chern-insulator model and examines how different mass-generating mechanisms, including magnetic exchange and spin-orbit coupling, can open gaps at Dirac points and produce quantum anomalous Hall phases in magnetic topological insulators, graphene-based systems, and ferromagnetic spin-gapless semiconductors. Their research establishes the broader physical relevance of Haldane-type Chern physics, but its objective is a perspective review of material and model realizations rather than a systematic numerical characterization of the Berry-curvature evolution and Chern-number transition of the minimal Haldane model itself.

Bhattacharjee et al. (2021) investigated a bilayer extension of the Haldane model consisting of two coupled Chern-insulating layers. Their study developed a topological characterization of the bilayer system, demonstrated that an appropriately defined Chern number can distinguish its different phases, and explicitly examined the associated bulk-boundary correspondence. They further considered adiabatic paths between Chern-inequivalent phases through variation of the interlayer coupling while maintaining a bulk gap. This research is relevant to the present study because it demonstrates how Chern-number classification and boundary-state behavior can be used together to characterize topological phases. However, its principal focus is the topology and adiabatic connectivity of a coupled bilayer system rather than the detailed numerical resolution of the phase transition in the fundamental single-layer Haldane model through simultaneous analysis of Berry curvature, bulk-gap closing, Chern-number quantization, and edge-state emergence.

Lü et al. (2025) examined graphene incorporating the Haldane model together with an extrinsic Rashba spin-orbit interaction, ferromagnetic exchange, and staggered potential. Their calculations produced a richer topological phase structure with Chern numbers extending beyond the $(C = \pm 1)$ phases of the minimal spinless Haldane model. They also calculated the corresponding edge states in zigzag graphene nanoribbons and investigated resonant tunneling associated with different chiral and mixed edge states. Their results demonstrate how additional physical interactions can substantially enrich the topological phase diagram and boundary-state structure of Haldane-based systems. These results, however, concern an extended model with Rashba coupling and exchange, and they do not establish how the transition behaves numerically in the minimal spinless model.

These studies demonstrate the continuing relevance of Haldane-type systems while also revealing a useful distinction for the present investigation. Recent work has increasingly emphasized material realizations, coupled or extended Haldane models, higher-Chern phases, and specialized forms of bulk-boundary correspondence. Each of these studies establishes the physics of the extended system it treats. None of them was designed to show how the geometric, spectral, topological, and boundary signatures of the transition behave together in the minimal Haldane model.

The topological transition in the Haldane model results from the competition between the staggered sublattice potential and the complex next-nearest-neighbor hopping. The staggered potential M produces opposite on-site energies on the two sublattices and favors a topologically trivial insulating phase, whereas the complex next-nearest-neighbor hopping introduces a phase-dependent contribution to the effective masses at the two inequivalent Dirac points. For the conventional Haldane Hamiltonian, the bulk gap closes when

$$M = \pm 3\sqrt{3}\, t_2 \sin\phi \qquad (1)$$

Where t_2 is the next-nearest-neighbor hopping amplitude and ϕ is its complex hopping phase.

The closing of the bulk gap marks the boundary between distinct topological sectors because the Chern number can change only when the occupied and unoccupied bands become degenerate. When the gap reopens after crossing a transition boundary, the system can enter a Chern insulating phase characterized by C=+1 or C=−1, whereas regions in which the contributions from the two valleys cancel correspond to the topologically trivial phase with C=0. The resulting phase structure provides a direct connection between the microscopic parameters of the Hamiltonian, the bulk energy spectrum, and the global topology of the occupied band.

Berry curvature provides a local momentum-space description of the geometric structure responsible for the topological classification. It measures the geometrical response of the Bloch eigenstates as crystal momentum varies across the Brillouin zone and, when integrated over the complete Brillouin zone, determines the Chern number (Xiao et al., 2010). In the Haldane model, the Berry curvature is particularly important near the inequivalent Dirac points, where the competition between the two mass terms controls the opening and closing of the bulk gap. Monitoring the Berry-curvature distribution

as M and ϕ are varied provides a local description of the geometric changes accompanying the topological transition, while the Chern number provides the corresponding global classification (Michel & Potthoff, 2022).

For numerical calculations, the discretization of the Brillouin zone introduces an important computational consideration because Bloch eigenvectors are defined only up to a momentum-dependent phase. Direct differentiation of numerically obtained eigenvectors can therefore introduce gauge-dependent numerical errors. The lattice-gauge formulation developed by Fukui, Hatsugai, and Suzuki (2005) provides a gauge-invariant method for evaluating Chern numbers on a discretized Brillouin zone without requiring a globally fixed gauge. This method is suitable for numerical investigations in which the Brillouin zone is represented by a finite momentum-space mesh and allows the quantization of the Chern number to be tested directly as the numerical resolution is increased.

The Chern number has a further physical significance through the bulk-edge correspondence. A non-zero bulk Chern number implies the existence of chiral boundary modes whose net propagation direction is determined by the topology of the bulk bands. The topological classification obtained from a periodic bulk Hamiltonian should have a corresponding manifestation in a system with an open boundary. The connection between bulk topological invariants and boundary-state winding was established in the quantum Hall framework by Hatsugai (1993) and has become a central principle of topological band theory. In Haldane-type systems, this correspondence can be investigated numerically by comparing the Chern number obtained from the periodic bulk Hamiltonian with the energy spectrum of a finite-width ribbon (Bhattacharjee et al., 2021; Cheng et al., 2024). Related experimental work has also demonstrated the connection between Berry curvature, Chern-number characterization, and topology-linked chiral boundary states in Chern bands (Chen et al., 2023).

Although the Haldane model is analytically well established, identifying a non-zero Chern number alone does not establish the numerical reliability of a calculation. The calculated invariant should converge toward integer values as the Brillouin-zone resolution is increased, the numerical phase boundary should agree with the analytical condition in Equation (1), the change in the Chern number should coincide with the closing and reopening of the bulk gap, and the non-trivial phase should exhibit the expected chiral boundary modes. This validation-oriented approach, in which computed observables are tested against analytical benchmarks, normalization and Hermiticity checks, and step-refinement convergence, is consistent with the practice adopted in earlier numerical work on coupled spin-1/2 systems (Ajayi, 2026).

The research gap addressed here is the lack of a single, consistent numerical study of the minimal Haldane model that tests the bulk gap, Berry curvature, Chern-number quantization, phase-boundary location, mesh convergence, and ribbon boundary spectrum together. The aim of this study is therefore to provide a numerical cross-validation of the well-established Haldane transition, not to report a new phase or a new transition. The Bloch Hamiltonian is diagonalized on a discretized Brillouin zone, the occupied-band Chern number is obtained with the Fukui-Hatsugai-Suzuki method and checked against a finite-difference curvature integral, the numerical phase boundaries are compared with Equation (1), and a finite-width zigzag ribbon is used to examine the edge spectrum.

MATERIALS AND METHODS

The research uses a numerical implementation of the Haldane model on a two-dimensional honeycomb lattice to characterize Chern-insulator phase transitions through a combined analysis of Berry curvature, Chern number, bulk-gap evolution, and bulk-edge correspondence. The model consists of spinless fermions occupying two inequivalent sublattices, denoted A and B, of a honeycomb lattice. Three principal terms are included: real nearest-neighbour hopping with amplitude t_1, complex next-nearest-neighbour hopping with amplitude$t_2 e^{\pm i\phi}$, and a staggered sublattice potential M. The corresponding real-space Hamiltonian is written as:

$$H = -t_1 \sum_{\langle i,j\rangle} (\, c_i^{\dagger} c_j + \text{h. c.}\,) + t_2 \sum_{\langle\langle i,j\rangle\rangle} (\, e^{i\nu_{ij}\phi} c_i^{\dagger} c_j + \text{h. c.}\,) + M \sum_i \xi_i \, c_i^{\dagger} c_i \qquad (2)$$

Where $c_i^{\dagger}$ and c_i are fermionic creation and annihilation operators, respectively. The symbol $\langle i,j\rangle$ denotes nearest-neighbour pairs, whereas $\langle\langle i,j\rangle\rangle$ denotes next-nearest-neighbour pairs. The factor $\nu_{ij} = \pm 1$ specifies the orientation of the next-nearest-neighbour hopping around the elementary plaquettes (vij = +1 for a hop from j to i that circulates counter-clockwise around a hexagon and −1 for a clockwise hop), thereby introducing the complex phase responsible for time-reversal-symmetry breaking. The sublattice factor is $\xi_i = +1$ on sublattice A and $\xi_i = -1$ on sublattice B. Throughout the calculations, the nearest-neighbour hopping amplitude is used as the energy scale, such that t_1=1. All energies and model parameters are expressed in dimensionless units relative to t_1. The independent parameters controlling the topological structure are therefore$M/t_1, t_2/t_1, and\ \phi$.

Lattice Geometry and Conventions

Lengths are measured in units of the nearest-neighbour distance a=1. The primitive lattice vectors are a_1=(√3, 0) and a_2=(√3/2, 3/2), and the reciprocal vectors G_1 and G_2 satisfy $G_i \cdot a_j = 2\pi\delta_{ij}$. The three nearest-neighbour vectors from a site of sublattice A to its neighbours on sublattice B are δ_1=(0, 1), δ_2=(√3/2, −1/2), and δ_3=(−√3/2, −1/2).

The three next-nearest-neighbour vectors are $b_1=-a_1$, $b_2=a_2$, and $b_3=a_1-a_2$; they are ordered counter-clockwise and are 120° apart. The Bloch Hamiltonian below is written in the basis that includes the positions of the two sublattice sites inside the cell, so that its off-diagonal element contains the phases $e^{ik\cdot\delta_j}$. Momentum is given either by Cartesian components $k=(k_x, k_y)$ or by the reciprocal coordinates $q_i=k\cdot a_i$, which run from 0 to 2π across the Brillouin zone. The two inequivalent Dirac points are $K=(4\pi/3\sqrt{3}, 0)$ and $K'=-K$, which correspond to $(q_1, q_2)=(4\pi/3, 2\pi/3)$ and $(2\pi/3, 4\pi/3)$, respectively. The high-symmetry path used for the band structures is $\Gamma\rightarrow K\rightarrow M\rightarrow\Gamma$, with $\Gamma=(0, 0)$ and $M=(\pi/\sqrt{3}, \pi/3)$.

Bloch Hamiltonian

Using translational symmetry, the real-space Hamiltonian is transformed into momentum space in the two-sublattice basis (A, B). The Bloch Hamiltonian is expressed in terms of Pauli matrices as

$$H(\mathrm{k}) = d_0(\mathrm{k})I + d_x(\mathrm{k})\sigma_x + d_y(\mathrm{k})\sigma_y + d_z(\mathrm{k})\sigma_z \quad (3)$$

Equivalently,

$$H(\mathrm{k}) = d_0(\mathrm{k})I + \mathrm{d}(\mathrm{k})\cdot\sigma \quad (4)$$

Where

$$\mathrm{d}(\mathrm{k}) = [d_x(\mathrm{k}), d_y(\mathrm{k}), d_z(\mathrm{k})] \quad (5)$$

The nearest-neighbour structure factor is defined as

$$f(\mathrm{k}) = \sum_{j=1}^{3} e^{i\mathrm{k}\cdot\delta_j} \quad (6)$$

Where δ_j (j = 1, 2, 3) are the three nearest-neighbour vectors defined above. The corresponding components are

$$d_x(\mathrm{k}) = -t_1 Ref(\mathrm{k}) \quad (7)$$

And

$$d_y(\mathrm{k}) = t_1 Imf(\mathrm{k}) \quad (8)$$

The next-nearest-neighbour contribution is separated into a time-reversal-even and a time-reversal-odd component. With b_j denoting the three next-nearest-neighbour vectors defined above, these are written as

$$d_0(\mathrm{k}) = 2t_2\cos\phi\sum_{j=1}^{3}\cos(\mathrm{k}\cdot\mathrm{b}_j) \quad (9)$$

And

$$d_z(\mathrm{k}) = M - 2t_2\sin\phi\sum_{j=1}^{3}\sin(\mathrm{k}\cdot\mathrm{b}_j) \quad (10)$$

With the vectors δ_j and b_j defined above, the sign of the last term in d_z gives the effective masses $m_\pm$ listed below, and the occupied-band Chern number is $C=-1$ inside the topological interval. The same convention is retained throughout the bulk and ribbon calculations so that the sign of the calculated Chern number and the propagation direction of the edge modes remain internally consistent.

The resulting two-band energy spectrum is:

$$E_\pm(\mathrm{k}) = d_0(\mathrm{k}) \pm |\mathrm{d}(\mathrm{k})| \quad (11)$$

Where

$$|\mathrm{d}(\mathrm{k})| = \sqrt{d_x^2(\mathrm{k}) + d_y^2(\mathrm{k}) + d_z^2(\mathrm{k})} \quad (12)$$

The lower band $E_-(\mathbf{k})$ is regarded as occupied at half filling, while $E_+(\mathbf{k})$ represents the unoccupied band. For $\varphi=\pi/2$ the term d_0 vanishes, so the two bands are symmetric about E=0 and the direct and indirect gaps coincide. For other values of φ the term d_0 is non-zero and the indirect gap can be smaller than the direct gap.

Parameter-Space Investigation

The central numerical investigation examines the dependence of the topological phase on the staggered potential M, next-nearest-neighbour hopping t_2, and phase ϕ. The calculations are organized around the analytical Haldane transition condition.

$$M_c^{\pm} = \pm 3\sqrt{3}\,t_2\sin\phi \quad (13)$$

The corresponding effective masses at the two inequivalent Dirac points are

$$m_\pm = M \mp 3\sqrt{3}\,t_2\sin\phi \quad (14)$$

The transition occurs when either effective Dirac mass vanishes,

$$m_\pm = 0 \quad (15)$$

For each selected set of parameters, the Hamiltonian is evaluated over the first Brillouin zone and diagonalized numerically. The corresponding energy bands, Berry curvature, Chern number, and minimum bulk gap are calculated. The numerical phase boundaries are subsequently compared with Equation (13).

A principal phase diagram is constructed in the (M,ϕ) parameter plane for a fixed value of t_2/t_1. Additional one-dimensional parameter sweeps across the predicted critical values are used to resolve the transition in greater detail. The control-parameter step is refined in the vicinity of the transition to avoid missing the narrow region in which the bulk gap closes. The production scans use a mass step $\Delta M=0.01$ over the ranges shown in Figures 3 and 4. Near each boundary the step is reduced to 0.001, and the boundary is then located by bisection on the Chern number (Table 7).

Brillouin-Zone Discretization and Eigenstate Calculation

The first Brillouin zone is represented by a uniform two-dimensional momentum-space mesh of N×N points with periodic boundary conditions. Each momentum point is written as:

$$\mathrm{k}_{ij} = \frac{i}{N}\mathrm{G}_1 + \frac{j}{N}\mathrm{G}_2,\ \ i,j = 0,1,\ldots,N-1 \quad (16)$$

This mesh contains the Γ point and excludes the zone edge, which is identified with the opposite edge through periodicity, so indices are taken modulo N when neighbouring points are formed. When N is divisible by 3 the Dirac points K and K′ lie on the mesh. The production calculations use N=122, for which neither Dirac point is sampled exactly. This is why the finite-mesh gap minimum stays small but non-zero at the analytical critical mass.

At every point on the mesh, the Bloch Hamiltonian is diagonalized according to

$$H(\mathrm{k})|u_n(\mathrm{k})\rangle = E_n(\mathrm{k})|u_n(\mathrm{k})\rangle \quad (17)$$

Where n=-, + denotes the lower and upper bands, respectively. The eigenvectors are normalized according to

$$\langle u_n(\mathrm{k})|u_n(\mathrm{k})\rangle = 1 \quad (18)$$

The occupied-band eigenvectors $|u_{-}(\mathbf{k})\rangle$ are retained for the geometric and topological calculations.

Because the Chern number is an integer-valued quantity, an integer FHS result is not taken as evidence of convergence on its own. Convergence is documented through three quantities: the finite-difference Berry-curvature integral, which reaches the quantized value only as the mesh is refined; the minimum direct gap, which approaches the exact Dirac-point value; and the location of the Chern-number change, which approaches the analytical critical mass. The calculations are repeated on progressively finer meshes (N = 62, 122, 242, 482, and 962 for the FHS and gap calculations, and N_q = 41 to 121 for the continuous integral), and the results are reported in Table 2 and Table 7.

Berry Connection and Berry Curvature

The geometric properties of the occupied Bloch states are characterized using the Berry connection,

$$\mathrm{A}_n(\mathrm{k}) = i\langle u_n(\mathrm{k})|\nabla_{\mathrm{k}} u_n(\mathrm{k})\rangle \quad (19)$$

The corresponding Berry curvature is

$$\Omega_n(\mathrm{k}) = \nabla_{\mathrm{k}} \times \mathrm{A}_n(\mathrm{k}) \quad (20)$$

For the two-dimensional system, the relevant component is

$$\Omega_n(\mathrm{k}) = \frac{\partial A_{n,y}}{\partial k_x} - \frac{\partial A_{n,x}}{\partial k_y} \quad (21)$$

For the two-band Hamiltonian, the Berry curvature can alternatively be expressed directly in terms of the normalized pseudospin vector,

$$\hat{\mathrm{d}}(\mathrm{k}) = \frac{\mathrm{d}(\mathrm{k})}{|\mathrm{d}(\mathrm{k})|} \quad (22)$$

As

$$\Omega_{\pm}(\mathrm{k}) = \mp\frac{1}{2}\hat{\mathrm{d}}(\mathrm{k}) \cdot \left[\frac{\partial \hat{\mathrm{d}}}{\partial k_x} \times \frac{\partial \hat{\mathrm{d}}}{\partial k_y}\right] \quad (23)$$

Berry-curvature maps are obtained for representative parameter points selected from the trivial phase, the vicinity of the transition, and the Chern-insulating phase. Particular attention is given to the neighbourhood of the two inequivalent Dirac points, where the curvature becomes strongly modified as the corresponding Dirac masses approach zero. In this convention the occupied band has $\Omega_{-} = +(1/2)\,\hat{\mathrm{d}}\cdot(\partial\hat{\mathrm{d}}/\partial \mathrm{k_x} \times \partial\hat{\mathrm{d}}/\partial \mathrm{k_y})$, and the Chern number counts how many times $\hat{\mathrm{d}}$ covers the unit sphere.

Numerical Chern-Number Calculation

The Chern number of the occupied band is defined in the continuum by

$$C = \frac{1}{2\pi}\int_{\mathrm{BZ}} \Omega_{-}(\mathrm{k})\, d^2\mathrm{k} \quad (24)$$

For the numerical calculation, a gauge-invariant discretized Brillouin-zone formulation is adopted. Specifically, the Fukui-Hatsugai-Suzuki method is used because it avoids the need to impose a globally smooth gauge on the numerically calculated eigenvectors.

For neighbouring momentum points, the normalized link variable in direction μ = x, y is defined as follows, with $\Delta k_x = G_1/N$, $\Delta k_y = G_2/N$, and indices taken modulo N:

$$U_{\mu}(\mathbf{k}) = \frac{\langle u_{-}(\mathbf{k})|u_{-}(\mathbf{k}+\Delta k_{\mu})\rangle}{|\langle u_{-}(\mathbf{k})|u_{-}(\mathbf{k}+\Delta k_{\mu})\rangle|} \quad (25)$$

The lattice field strength associated with each elementary plaquette is

$$F_{xy}(\mathbf{k}) = \ln\left[U_x(\mathbf{k})U_y(\mathbf{k}+\Delta k_x)U_x^{-1}(\mathbf{k}+\Delta k_y)U_y^{-1}(\mathbf{k})\right] \quad (26)$$

The principal-valued lattice Berry flux is then The minus sign is needed for consistency with the convention A = i⟨u|∇u⟩ used above. The plaquette product in Equation (26) is the original Fukui-Hatsugai-Suzuki form, which is built from A = ⟨u|∇u⟩ and gives a flux of opposite sign. With the definition in Equation (27), the lattice flux and the continuous curvature of Equation (23) give the same sign of C at every parameter point tested.

$$\mathcal{F}_{xy}(\mathbf{k}) = -ImF_{xy}(\mathbf{k}) \quad (27)$$

The numerical Chern number is obtained from

$$C = \frac{1}{2\pi}\sum_{\mathbf{k}} \mathcal{F}_{xy}(\mathbf{k}) \quad (28)$$

The calculated Chern number is monitored as the momentum-space mesh is refined. Integer values are interpreted as reliable only when they are stable under mesh refinement and the corresponding bulk spectrum remains gapped.

Bulk-Gap Calculation

The direct energy gap at each momentum point is calculated from

$$\Delta(\mathbf{k}) = E_{+}(\mathbf{k}) - E_{-}(\mathbf{k}) \quad (29)$$

The minimum bulk gap is then determined from

$$\Delta_{\mathrm{bulk}} = \min_{\mathbf{k}\in\mathrm{BZ}}[E_{+}(\mathbf{k}) - E_{-}(\mathbf{k})] \quad (30)$$

The momentum at which the minimum occurs is also recorded. At the topological phase transition, the bulk gap is expected to approach zero,

$$\Delta_{\mathrm{bulk}} \to 0 \quad (31)$$

And subsequently reopen as the system enters the neighbouring insulating phase.

The numerical gap minimum is compared with the locations of the inequivalent Dirac points. The direct gap Δ(k) is distinguished from the indirect (global) gap E_g = min $E_{+}(k)$ − max $E_{-}(k)$. For φ=π/2 the term d_0 vanishes, so $E_g = \Delta_{\mathrm{bulk}}$. The common projected gap used for the ribbon spectra is defined from E_g.

Numerical Determination and Validation of the Phase Boundary

The numerical transition point M_c^{num} is obtained by resolving the parameter value at which the minimum bulk gap approaches zero and the Chern number changes between neighbouring insulating regions. This value is compared with the analytical prediction

$$\epsilon_c = \frac{|M_c^{\text{num}} - M_c^{\text{anal}}|}{|M_c^{\text{anal}}|} \times 100\% \quad (32)$$

The numerical phase boundary is considered satisfactorily resolved only when there is a minimum of the bulk gap at the predicted transition, a change in the Chern number across the transition, and agreement between the numerical and analytical critical parameters within the established numerical resolution. The resolution of a scan is set by its mass step ΔM, and each boundary is then refined by bisection on the Chern number.

Chern-Number Phase Diagram

A two-dimensional phase diagram is constructed by evaluating the Chern number over a systematic grid in the selected parameter plane. Each point is accompanied by its corresponding minimum bulk gap.

The trivial insulating phase is identified by

C=0,

Whereas the nontrivial Chern-insulating phases of the minimal model are characterized by

C=±1.

The calculated Chern-number regions are compared with the analytical phase boundaries. The sign of the Chern number depends on the adopted orientation and phase convention for the honeycomb lattice.

Finite-Ribbon Calculation and Bulk-Edge Correspondence

The bulk calculation is complemented by a finite-ribbon calculation in order to test the bulk-edge correspondence directly. Periodic boundary conditions are retained along the longitudinal direction a_1 of the ribbon, whereas the transverse direction is made finite. The ribbon has zigzag edges and contains $N_y = 40$ unit cells along a_2 (80 sites), so that it ends on an A-terminated edge (left) and a B-terminated edge (right). The longitudinal momentum $k_\parallel$ is sampled at $N_k = 401$ points spanning one period, $-\pi/\sqrt{3} \le k_\parallel \le \pi/\sqrt{3}$, and the full spectrum therefore contains $2N_yN_k = 32{,}080$ states.

For a ribbon containing N_y transverse unit cells, the Hamiltonian is written as:

$$H_{\text{rib}}(k_\parallel) = \sum_{n=1}^{N_y} \Psi_n^\dagger H_0(k_\parallel)\Psi_n + \sum_{n=1}^{N_y-1}\left[\Psi_n^\dagger T(k_\parallel)\Psi_{n+1} + \text{H. c.}\right] \quad (33)$$

For each longitudinal momentum $k_\parallel$, the ribbon Hamiltonian is diagonalized according to

$$H_{\text{rib}}(k_\parallel)|\psi_\alpha(k_\parallel)\rangle = E_\alpha(k_\parallel)|\psi_\alpha(k_\parallel)\rangle \quad (34)$$

The resulting energy spectrum is examined for states crossing the projected bulk gap. For each eigenstate, the probability density is: The common projected bulk gap is the interval $|E| < 0.18\ t_1$. It is the intersection of the bulk gaps of the two phases compared here, $|E| < 0.2196\ t_1$ for $M = 0.3$ and $|E| < 0.1804\ t_1$ for $M = 0.7$, obtained from the bulk spectrum over the whole Brillouin zone.

$$\rho_\alpha(n) = \sum_{s=A,B} |\psi_{\alpha,n,s}|^2 \quad (35)$$

The boundary localization weight is calculated from:

$$P_{\text{edge}}^{(\alpha)} = \sum_{n\in\mathcal{E}} \rho_\alpha(n) \quad (36)$$

Where $\mathcal{E}$ denotes a prescribed set of cells near either ribbon boundary. In the dispersion analysis, $\boldsymbol{\mathcal{E}}$ consists of the five outermost cells at each edge, P_L and P_R denote the weights on the left and right edges, and a state is called edge-localized when $P_L + P_R > 0.5$. The counts in Table 5 use the same edge region and threshold, with the energy window $|E| < 0.18\ t_1$. Table 8 shows how they change with the width of the window.

States with substantial boundary localization and energies within the projected bulk gap are identified as edge states. Their direction of dispersion is determined from the slope:

$$v_\alpha(k_\parallel) = \frac{1}{\hbar}\frac{\partial E_\alpha(k_\parallel)}{\partial k_\parallel} \quad (37)$$

For a nontrivial phase with |C|=1, the ribbon calculation is expected to reveal one net chiral edge channel per boundary, with opposite propagation directions on the two opposite edges. The edge-state spectrum is therefore used as an independent physical manifestation of the bulk Chern number. A nontrivial phase is accepted as a Chern-insulating phase only when the Chern number is quantized, the bulk spectrum is gapped away from the transition, the numerical result is converged, and the corresponding ribbon spectrum shows boundary-localized branches that cross the common projected gap with opposite velocities on the two edges. Localization counts alone are not accepted as evidence of chirality.

All numerical calculations are performed using a consistent computational workflow on Python in which the same model parameters, lattice convention, hopping amplitudes, phase convention, and energy normalization are used throughout the bulk and ribbon calculations. The numerical procedure consists of constructing the Bloch Hamiltonian, diagonalizing it throughout the Brillouin zone, evaluating the Berry curvature and Chern number, determining the minimum bulk gap, locating and validating the phase boundary, and finally constructing and diagonalizing the corresponding finite ribbon. The calculations are repeated at selected parameter points and different numerical resolutions to establish reproducibility. The final reported phase boundaries, Chern numbers, Berry-curvature distributions, bulk gaps, and edge spectra are retained together so that the principal conclusions can be independently reproduced from the same parameter set. Matlab is used for visualizations.

The computational procedure is summarized by the following steps.

Step 1. Fix $t_1 = 1$, $t_2 = 0.1$, $\varphi = \pi/2$, and the vectors a_j, δ_j, and b_j given above.

Step 2. For each mass M in the scan, build H(k) on the N×N periodic mesh$kij = (i/N)G1 + (j/N)G2$ and diagonalize it to obtain $E \pm (k) and |u - (k)\rangle$.

Step 3. Form the link variables U_x and U_y, the plaquette flux $Fxy = -Imln[Ux(k)Uy(k + \Delta kx)Ux - 1(k + \Delta ky)Uy - 1(k)], andC = (1/2\pi)\Sigma Fxy.$

Step 4. Evaluate the continuous Berry-curvature integral on an $N_q \times N_q$ mesh using second-order central finite differences of $\hat{d}(k)$ (not analytic derivatives) and $\Omega - = +(1/2)\hat{d} \cdot (\partial x\hat{d} \times \partial y\hat{d})$.
Step 5. Record $\Delta bulk = mink[E + (k) - E - (k)]$ its momentum, and the exact gaps at K and K′.
Step 6. Bracket each boundary between adjacent scan points where C changes, refine it by bisection on C, and compare the result with $Mc = \pm 3\sqrt{3}t2sin\varphi$.
Step 7. Build the zigzag ribbon with $N_y = 40$, diagonalize $H_{rib}(k_\parallel)$ at $N_k = 401$ values of $k_\parallel$, and compute E_α, P_L, P_R, and v_α for every eigenstate.
Step 8. Repeat Steps 2 to 7 for the mesh sizes listed in Table 7.

RESULTS AND DISCUSSION

The numerical results establish a consistent connection between the bulk spectral structure, Berry curvature, Chern-number quantization, phase-boundary location, and boundary-state response of the Haldane model. The production calculation uses t1 = 1, t2 = 0.1, and φ = π/2, for which the analytical critical masses are M_c- = −0.519615242 and M_c+ = +0.519615242. The discussion below focuses on the representative insulating phases, the evolution of the bulk gap across the transition, the geometric origin of the Chern invariant, and the independent numerical checks used to establish the reliability of the classification. The sign of the reported Chern number follows the occupied-band and lattice-orientation convention used consistently in the bulk and ribbon calculations; consequently, the physically important distinction is between the topologically non-trivial sector and the trivial sector, while the sign fixes the associated orientation convention for the edge response.
Figure 1 shows the representative bulk band structures for M = −0.3, M = 0.3, and M = 0.7 along the selected high-symmetry momentum path. The three calculations remain insulating, but their topological classification is different. For M = −0.3 and M = 0.3, the lower and upper bands remain separated by a finite direct gap, whereas the M = 0.7 spectrum represents the positive-mass trivial regime. The numerical minimum direct gaps and the corresponding Chern classifications are summarized in Table 1. The two topological representatives have the same minimum direct gap, 0.4428937 in the production calculation, and both have C = −1 under the adopted convention. This equality follows from the symmetry of the model at φ = π/2: the transformation (M, k) → (−M, −k) maps the d-vector to (d_x, $-d_y$, $-d_z$), which preserves |d| and the orientation of the map, so the minimum gap and the Chern number are the same for M = −0.3 and M = 0.3. The M = 0.7 state has a minimum direct gap of 0.36589298 and C = 0. Thus, the difference between the representative phases is not the mere presence or absence of a spectral gap: all three selected points are gapped. Rather, it is the global topology of the occupied band that distinguishes the two regimes. This distinction is central to the Chern-insulator description because a nonzero Chern number cannot be inferred from a finite gap alone.

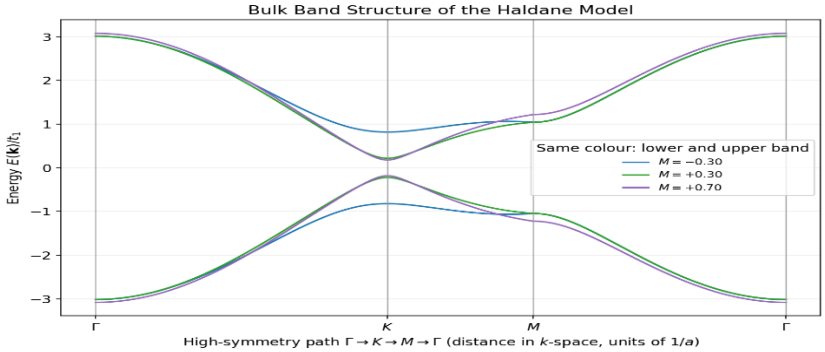


Figure 1: Representative bulk band structures of the Haldane model for M = −0.3, 0.3, and 0.7 along the path Γ → K → M → Γ, with Γ = (0, 0), K = (4π/3√3, 0), and M = (π/√3, π/3) in units of 1/a. For each value of M the lower and upper bands share one colour, and energies are in units of t_1

Table 1: Representative Bulk Phases and their Numerical Topological Classification, Gaps are Evaluated on the 122 × 122 Mesh

Phase	M	Chern number	Minimum direct gap
Topological negative-M	−0.3	−1	0.4428937
Topological positive-M	+0.3	−1	0.4428937
Trivial positive-M	+0.7	0	0.3658930

Figure 2 shows the gauge-invariant Berry-curvature maps for the same representative sectors together with a point just above the positive critical mass. The topological cases show pronounced localized Berry-curvature structure in the vicinity of the inequivalent Dirac regions, while the trivial state at M = 0.7 exhibits a distribution whose Brillouin-zone integral is consistent with zero. The calculation therefore provides the local geometric information that underlies the global Chern classification. At M = 0.529615242, just above M_c+, the curvature pattern is strongly modified in the transition neighbourhood, but the system has already entered the trivial sector. This is important because it demonstrates that a visibly concentrated Berry-curvature feature near a Dirac valley should not by itself be interpreted as evidence of a nonzero Chern number; the full Brillouin-zone integral and the bulk gap must be considered together.

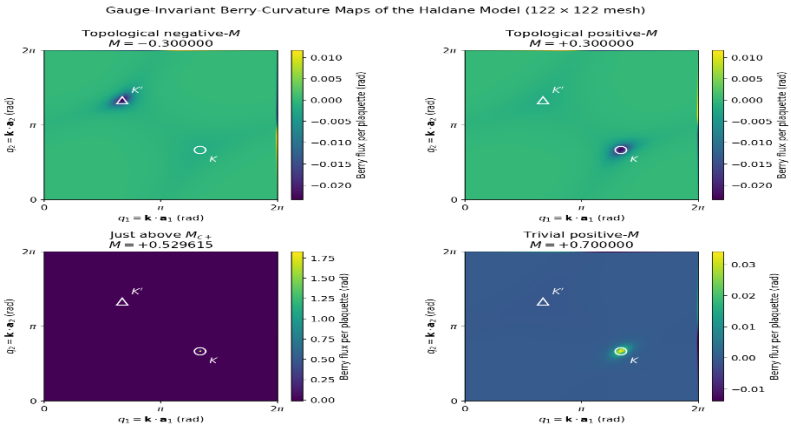


Figure 2: Gauge-invariant Berry-flux maps (flux per plaquette of the 122 × 122 mesh) for representative topological, near-transition, and trivial parameter regimes. The axes are the reciprocal coordinates $q_i = k \cdot a_i$; circles mark K and triangles mark K′

Table 2: Independent Continuous-Berry and Fukui-Hatsugai-Suzuki Chern-Number Validation. The Continuous Values Use Second-Order Central Finite Differences of $\hat{D}$ (K) On an $N_q \times N_q$ Mesh; the FHS Values Use the 122 × 122 Mesh

M	Expected/phase Chern	Continuous Berry Chern (Nq = 101)	FHS Chern	Validation
−0.3	−1	−0.993023952	−1	Integer agreement
+0.3	−1	−0.993023952	−1	Integer agreement
+0.7	0	−0.006514831	0	Integer agreement

Table 2 shows an independent numerical check on the lattice-gauge result. At Nq = 101, the continuous Berry-curvature integral gives −0.993023952 for both representative topological phases, which approaches the quantized value −1, while the trivial phase gives −0.006514831, which approaches zero. The FHS calculation returns the corresponding integer values exactly, namely −1, −1, and 0. The agreement is therefore not dependent on a single numerical formulation. This cross-validation is particularly important because the Berry connection is gauge dependent and direct numerical differentiation of eigenvectors can be sensitive to discretization and gauge choices. The FHS lattice-gauge formulation was designed to avoid that problem, while the continuous calculation provides an independent geometric check. The continuous calculation differentiates the normalized d-vector with second-order central finite differences, not with analytic derivatives, so its deviation from the integer is a discretization error that falls roughly as $1/Nq^2$. The mesh-convergence calculations, retained in the supplementary material, show that the continuous topological values move systematically toward the integer sectors as the Brillouin-zone resolution is increased. For the topological phase the continuous estimate changes from approximately −0.96085 at Nq = 41 to −0.99511 at Nq = 121, while the integer classification remains −1. For the trivial phase, the continuous value moves from approximately −0.03348 to −0.00459 over the same refinement range, with integer classification remaining zero. This behaviour is consistent with a converged topological invariant rather than a mesh-dependent numerical artefact. Because the FHS result is an integer on every mesh tested, it does not demonstrate convergence by itself, and the convergence of the gap minimum and of the boundary location is documented in Table 7.

The spectral signature of the phase transition is shown in Figure 3. As M is varied, the minimum direct bulk gap

decreases toward both analytical transition masses and reopens on the opposite side of each transition. The gap is largest near M = 0 and decreases symmetrically toward the two critical regions. The numerical scan therefore reproduces the expected structure in which the insulating phases are separated by gap-closing points. The scan in Figure 3 uses the 122 × 122 mesh and a mass step of 0.01. This mesh does not place a point on the Dirac valley at the analytical critical mass (122 is not divisible by 3), so the plotted finite-mesh minimum remains small but nonzero near the critical parameter, at 0.059 for M = ±0.52, whereas the exact Dirac-point gap, shown as the dotted curve, vanishes at the critical masses. This is a resolution issue rather than a failure of the analytical transition condition. The exact valley calculation provides the decisive check: the gap closes at K′ for M_c- and at K for M_c+ to numerical precision, as reported later in Table 4.

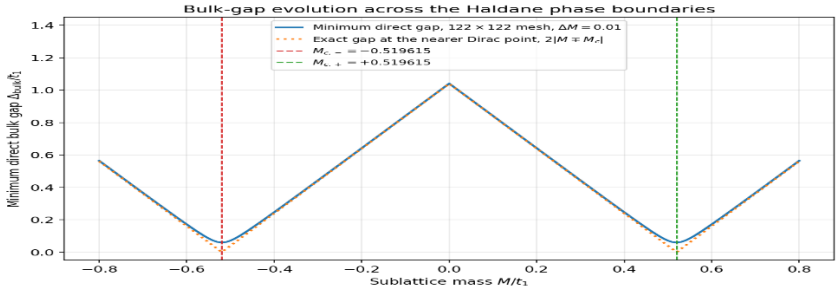


Figure 3: Evolution of the minimum direct bulk gap across the Haldane phase boundaries, computed on the 122 × 122 mesh with ΔM = 0.01 (solid), compared with the exact gap at the nearer Dirac point (dotted)

Figure 4 shows the resulting Chern-number sectors across the mass parameter. The calculation gives a trivial phase with C = 0 for M below Mc−, a non-trivial interval with C = −1 between the two critical masses, and a second trivial phase with C = 0 for M above Mc+. The transition points themselves are gapless and therefore are not assigned a Chern number in the production classification. This treatment is essential: the Chern invariant is a property of a gapped occupied band and is not defined at the band-degeneracy point where the bulk gap closes. The agreement between the Chern classification and the gap evolution in Figure 3 provides a direct spectral-topological consistency check. The topological interval is also consistent with the analytical competition between the staggered mass and the time-reversal-breaking next-nearest-neighbour contribution. The numerical result therefore reproduces the characteristic Chern-insulating window of the minimal Haldane model rather than merely producing isolated nonzero Chern values at selected parameter points.

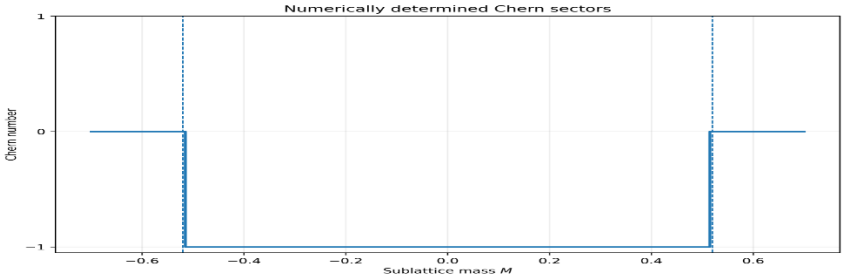


Figure 4: Numerically determined Chern-number sectors as a function of the staggered sublattice potential M

The quantitative agreement between analytical and numerical phase boundaries is shown in Figure 5 and Table 3. The analytical values are M_c- = −0.519615242 and M_c+ = +0.519615242, whereas the grid-resolved transition locations are approximately −0.52 and +0.52. The absolute discrepancy is 0.000384758 for each boundary, corresponding to a relative difference of only 0.07405%. Because the numerical transition is resolved on a discrete parameter grid, this difference is appropriately interpreted as the parameter resolution of the numerical localization rather than as a systematic displacement of the physical transition. The scan step is ΔM = 0.01, so each boundary is only bracketed by two adjacent scan points (−0.52 and −0.51 for M_c-, and 0.51 and 0.52 for M_c+), and the grid-resolved value is the scan point nearest to the boundary. The quoted discrepancy is therefore a grid-localization effect with an uncertainty of the order of ΔM, and it is not a physical model error.

Reducing the step to 0.001 narrows the bracket to the interval between 0.519 and 0.520, and bisection on the FHS Chern number places the boundary within 1.8e-04 of the analytical value on the 122 × 122 mesh and within 3.0e-06 on the 962 × 962 mesh (Table 7). The phase classifications immediately on the two sides of the boundaries also change as expected: C = 0 below M_c- becomes C = −1 above M_c-, while C = −1 below M_c+ becomes C = 0 above M_c+. Thus, the numerical boundary is simultaneously supported by the parameter scan, the Chern-number change, and the exact Dirac-point calculation.

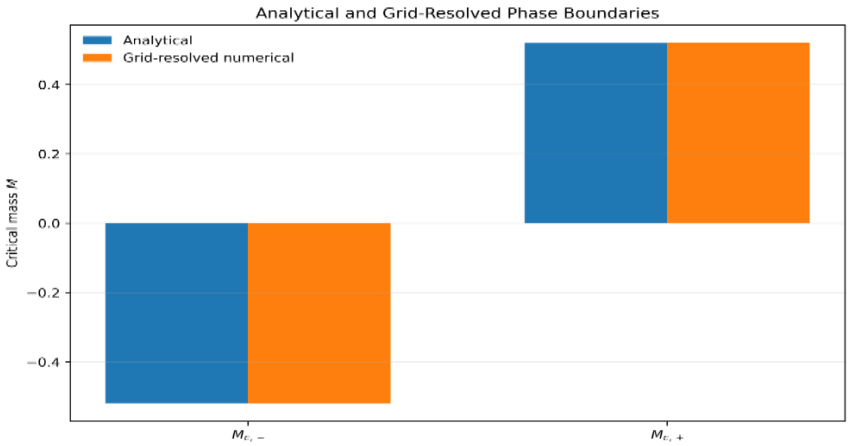


Figure 5: Comparison of the analytical Haldane critical masses with the grid-resolved numerical transition locations

Table 3: Analytical and Numerical Phase-Boundary Comparison

Boundary	Analytical M	Grid-resolved M	Absolute error	Relative error (%)	Closing valley	C below → C above
Mc−	−0.519615242	−0.52	0.000384758	0.07405	K′	0 → −1
Mc+	+0.519615242	+0.52	0.000384758	0.07405	K	−1 → 0

The microscopic location of each transition is independently verified by evaluating the Hamiltonian directly at the two inequivalent Dirac points. Table 4 shows that at M_c- the K′ valley closes with a gap of 8.88 × 10−16, while the K valley remains separated by a gap of 2.07846097. At M_c+ the roles are reversed: the K valley closes to 8.88 × 10−16 while K′ remains gapped by 2.07846097. These values are numerically consistent with exact band degeneracy to machine precision. The result is physically important because the Haldane transition is controlled by the competition of the effective masses at the two valleys; the topological change occurs when one valley mass changes sign and its Dirac gap closes. The gap then reopens on crossing the boundary, allowing the Chern number to change without contradicting its invariance under continuous deformations of a gapped Hamiltonian.

Table 4: Exact Dirac-Point Gap Closures at the Two Topological Phase Boundaries

Boundary	M	Closing valley	Gap at K	Gap at K′	Exact closing gap
Mc−	−0.519615242	K′	2.07846097	8.88 × 10−16	8.88 × 10−16
Mc+	+0.519615242	K	8.88 × 10−16	2.07846097	8.88 × 10−16

The bulk-edge calculation provides the final physical check. The finite ribbon uses the same lattice convention and production parameters as the bulk calculation, with M = 0.3 representing the topological sector and M = 0.7 representing the trivial sector. Table 5 shows that both ribbon calculations contain 32,080 states in the full numerical spectrum, of which 668 (M = 0.3) and 632 (M = 0.7) are edge-localized when the whole spectrum is counted. These totals are similar and should not be interpreted by themselves as evidence of topology, because the ribbons carry boundary-weighted states of the band continuum in both phases. The physically relevant comparison is inside the common projected gap, $|E| < 0.18\ t_1$. For M = 0.3, 202 states lie inside this window and all 202 are edge-localized. For M = 0.7, no state lies inside it. These are localization counts. They depend on the grid size, the energy window, and the localization threshold, and they do not show by themselves that a branch crosses the gap or in which direction it propagates. That is examined from the ribbon dispersion in Figure 7 and Table 6.

Table 5: Localization Counts for the Topological and Trivial Ribbons (N_y = 40, N_k = 401). A State Is Edge-Localized When $P_L + P_R > 0.5$ over Five Cells per Edge; the Window Is the Common Projected Gap, $|E| < 0.18$ T_1

Phase	M	Total states	Edge-localized states	States in common gap	Edge-localized states in common gap
Topological	0.3	32080	668	202	202
Trivial	0.7	32080	632	0	0

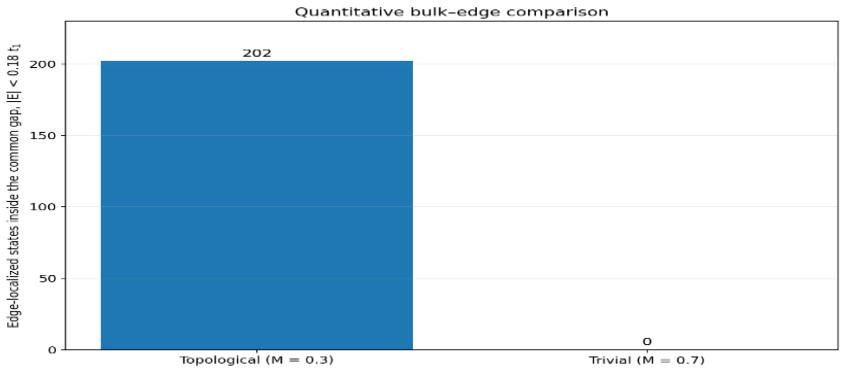


Figure 6: Edge-localized states inside the common projected bulk gap ($|E| < 0.18$ t_1) for the topological and trivial ribbon calculations

Figure 6 visualizes the in-gap localization counts reported in Table 5: 202 edge-localized states for the M = 0.3 ribbon and none for the M = 0.7 ribbon. This is consistent with the nonzero bulk Chern number obtained from the periodic bulk calculation. A count of this kind cannot establish chirality, because it does not show that a branch crosses the gap or in which direction it propagates. Figure 6 and Table 5 are therefore read as a first indication, and the evidence for bulk-edge correspondence is taken from the ribbon dispersion in Figure 7.

Figure 7 shows the ribbon dispersion $E(k_\parallel)$ for the same two ribbons. Each state is coloured by the difference between its weight on the A-terminated (left) edge and on the B-terminated (right) edge. For M = 0.3, two branches cross the common projected bulk gap and merge with the valence and conduction bands near the projected Dirac point at $k_\parallel \approx -1.2$. One branch is localized on the left edge and has a positive velocity, and the other is localized on the right edge and has a negative velocity. Both cross E = 0 at $k_\parallel \approx -0.63$ with velocities of v = +0.394 and v = −0.394 (in units of $t_1 a/\hbar$). Each edge therefore carries one chiral channel, and the net number of channels per edge is one, as required for |C| = 1. For M = 0.7 no eigenvalue lies inside the common gap, and the boundary-weighted branches that are visible stay outside it, attached to the band edges.

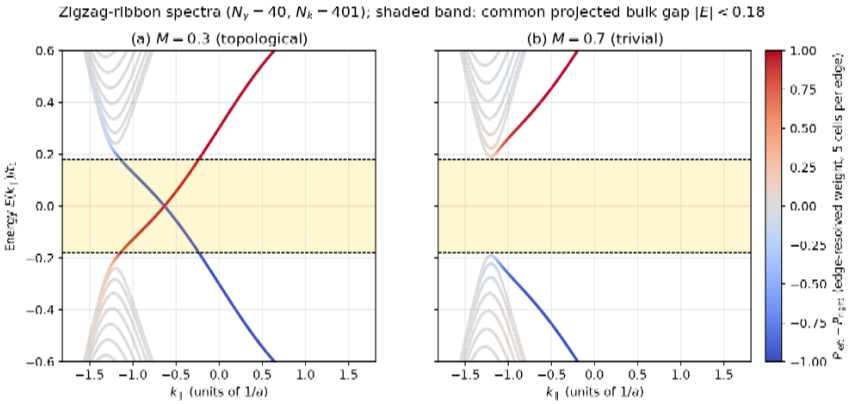


Figure 7: Zigzag-ribbon spectra $E(k_\parallel)$ for (a) M = 0.3 and (b) M = 0.7 (N_y = 40, N_k = 401). Each state is coloured by $P_L - P_R$, the difference between its weights on the left (A-terminated) and right (B-terminated) edges, computed over the five outermost cells at each edge. The shaded band is the common projected bulk gap, $|E| < 0.18$ t_1

Table 6: Ribbon Edge-Mode Indicators in the Common Projected Bulk Gap, $|E| < 0.18\ T_1$ ($N_y = 40$, $N_k = 401$). Velocities $V = \partial E/\partial K_\parallel$ are in Units of $T_1 a/\hbar$

Phase	M	Bulk gap half-width	States in common gap	Edge-localized states in common gap	v at E = 0, left edge	v at E = 0, right edge
Topological	0.3	0.2196	202	202	+0.394	−0.394
Trivial	0.7	0.1804	0	0	none	none

Table 7 documents the mesh refinement. For each FHS mesh size N it lists the Chern numbers at M = 0.3 and M = 0.7, the minimum direct gap at M = 0.3, and the critical mass M_c+ found by bisection on the Chern number, together with its deviation from the analytical value. The Chern numbers are −1 and 0 on every mesh, so they do not indicate convergence by themselves. The quantities that converge are the gap minimum, which approaches the exact Dirac-point value $2|M - M_c| = 0.4392305$, and the boundary location, whose deviation from the analytical M_c falls from 0.137% at N = 62 to 0.00057% at N = 962, in proportion to N^{-2}. At $\varphi = \pi/2$ the negative boundary M_c- is the mirror image of M_c+ and gives identical deviations.

Table 7: Mesh Refinement of the FHS Calculation ($T_1 = 1$, $T_2 = 0.1$, $\Phi = \Pi/2$). The Critical Mass Is Found By Bisection on the Chern Number; the Analytical Value is $M_c+ = 0.5196152$

N	C (M = 0.3)	C (M = 0.7)	Min. direct gap (M = 0.3)	M_c+ from bisection	$\|\Delta M_c\|$	Relative deviation (%)
62	−1	0	0.4530996	0.5189056	7.10e-04	0.13658
122	−1	0	0.4428937	0.5194317	1.84e-04	0.03532
242	−1	0	0.4401696	0.5195686	4.67e-05	0.00898
482	−1	0	0.4394681	0.5196035	1.18e-05	0.00227
962	−1	0	0.4392902	0.5196123	2.96e-06	0.00057

Table 8 shows how the counts depend on the width of the energy window, with the five-cell edge region and the 0.5 threshold of Table 5. While the window stays inside the common gap ($|E| \leq 0.18\ t_1$), the topological ribbon contains only edge-localized states and the trivial ribbon contains none. Once the window extends beyond the bulk band edge of the trivial phase ($0.1804\ t_1$), the trivial ribbon acquires states inside the window (38 at $|E| < 0.22\ t_1$ and 96 at $|E| < 0.25\ t_1$), of which a few are boundary-weighted (4 and 20), and the topological ribbon acquires bulk-continuum states that are not edge-localized (4 and 34). These states belong to the band continuum. They do not form a branch that crosses the gap, so they are best regarded as non-topological boundary-weighted states (surface resonances) and not as chiral edge modes. A small non-zero count in the trivial phase therefore cannot be used as a measure of topology, and it appears whenever the counting window is wider than the gap. With the window fixed at $|E| < 0.18\ t_1$, the in-gap counts are unchanged for thresholds from 0.3 to 0.7 and for edge regions of three to eight cells, and the M = 0.3 count falls to 186 at a threshold of 0.9.

Table 8: Dependence of the In-Window Counts On the Width of the Energy Window ($N_y = 40$, $N_k = 401$; Five Edge Cells, Threshold $P_L + P_R > 0.5$)

Window, |E| <	M = 0.3: states in window	M = 0.3: edge-localized	M = 0.7: states in window	M = 0.7: edge-localized
0.10	112	112	0	0
0.14	158	158	0	0
0.18	202	202	0	0
0.22	238	234	38	4
0.25	282	248	96	20
0.30	378	268	196	50

The results form a mutually consistent numerical characterization of the Haldane Chern-insulator transition. Figure 1 establishes the representative gapped bulk spectra, while Table 1 shows that the two topological representatives carry the same nonzero Chern invariant and the selected trivial representative carries C = 0. Figure 2 and Table 2 connect the local Berry-curvature geometry to the global topological invariant and demonstrate agreement between two independent numerical approaches. Figure 3 then shows the spectral mechanism of the transition through gap suppression and reopening, while Figure 4 demonstrates the corresponding change in the Chern sector. Figure 5 and Table 3 quantify the agreement between analytical and numerical transition locations, and Table 4 identifies the specific Dirac valley at which each gap closes. Table 5 and Figure 6 give localization counts for the finite ribbon, while Figure 7 and Table 6 show the chiral in-gap edge branches that connect the bulk invariant to the boundary. Table 7 documents the dependence of the gap minimum and the

boundary location on the Brillouin-zone resolution, and Table 8 shows how the localization counts depend on the width of the energy window.

The combined evidence also clarifies the role of each numerical diagnostic. A nonzero Chern number alone would establish a topological classification within the adopted convention, but it would not by itself demonstrate that the phase boundary has been correctly located or that the calculation is numerically converged. Here, the Chern result is supported by independent Berry-curvature integration, mesh refinement, bulk-gap evolution, exact Dirac-point closures, analytical-numerical boundary agreement, and a finite-ribbon edge-spectrum calculation. This layered validation is particularly appropriate for a computational study because it separates topological classification from numerical reliability. It also follows the physical logic established in the broader topological-band literature: Berry curvature supplies the geometric description, the Chern number supplies the global invariant, a bulk-gap closure permits a change of the invariant, and bulk-edge correspondence provides a boundary manifestation of the resulting topology. The results should therefore be interpreted as a systematic numerical cross-validation of the established minimal Haldane model rather than as a claim that the analytical phase diagram itself is newly discovered. The contribution of the present computation is the unified verification of the geometric, spectral, topological, convergence, and boundary signatures within one internally consistent parameter convention. Within the tested parameter set, the numerical evidence supports the identification of a Chern-insulating interval bounded by the two Dirac-point closures and flanked by trivial insulating sectors.

Conclusion

This study has provided a numerical cross-validation of the Chern-insulator transition in the minimal Haldane model within a single computational framework, with $t_1=1$, $t_2=0.1$, and $\phi=\pi/2$. The occupied band has Chern number $C=-1$ for $M=-0.3$ and $M=0.3$ and $C=0$ for $M=0.7$, which gives the sequence $C=0\rightarrow-1\rightarrow0$ across the two critical masses. The Fukui-Hatsugai-Suzuki result agrees with a finite-difference Berry-curvature integral, the critical masses $M\approx\pm0.52$ reproduce the analytical value ±0.519615 to within the scan resolution (relative discrepancy about 0.074%, with bisection converging toward the analytical value as the mesh is refined), and the exact Dirac-point calculation places the gap closure at K' for M_c- and at K for M_c+. In the zigzag ribbon, one chiral branch on each edge crosses the common projected bulk gap with opposite velocities for $M=0.3$, and no state lies in the gap for $M=0.7$, which is consistent with bulk-edge correspondence for $|C|=1$. The limits of these results are the finite Brillouin-zone and ribbon meshes, the single selected parameter set, and the dependence of the localization counts on the chosen energy window (Table 8), so those counts are supporting evidence only. A concrete extension is to map the full (M, ϕ) plane with the same procedure and to test the stability of the chiral edge branches in a disordered ribbon.

REFERENCES

Ajayi, I. O. (2026). Simulation of quantum spin systems for qubit applications. *Nigerian Journal of Applied Physics, 2*(3), 66–76. https://doi.org/10.62292/njap-v2i3-2026-94

Berry, M. V. (1984). Quantal phase factors accompanying adiabatic changes. *Proceedings of the Royal Society of London. A. Mathematical and Physical Sciences, 392*(1802), 45–57. https://doi.org/10.1098/rspa.1984.0023

Bhattacharjee, S., Bandyopadhyay, S., Sen, D., & Dutta, A. (2021). Bilayer Haldane system: Topological characterization and adiabatic passages connecting Chern phases. *Physical Review B, 103*(22), 224304. https://doi.org/10.1103/PhysRevB.103.224304

Chen, C., Liu, R.-Z., Wu, J., Su, Z.-E., Ding, X., Qin, J., Wang, L., Zhang, W.-W., He, Y., Wang, X.-L., Lu, C.-Y., Li, L., Sanders, B. C., Liu, X.-J., & Pan, J.-W. (2023). Berry curvature and bulk-boundary correspondence from transport measurement for photonic Chern bands. *Physical Review Letters, 131*(13), 133601. https://doi.org/10.1103/PhysRevLett.131.133601

Cheng, S., Jiang, Y., & Xianlong, G. (2024). Bulk-edge correspondence for the nonlinear eigenvalues problem of the Haldane model. *Physical Review B, 109*(13), 134201. https://doi.org/10.1103/PhysRevB.109.134201

Fukui, T., Hatsugai, Y., & Suzuki, H. (2005). Chern numbers in discretized Brillouin zone: Efficient method of computing (spin) Hall conductances. *Journal of the Physical Society of Japan, 74*(6), 1674–1677. https://doi.org/10.1143/JPSJ.74.1674

Haldane, F. D. M. (1988). Model for a quantum Hall effect without Landau levels: Condensed-matter realization of the "parity anomaly." *Physical Review Letters, 61*(18), 2015–2018. https://doi.org/10.1103/PhysRevLett.61.2015

Hatsugai, Y. (1993). Chern number and edge states in the integer quantum Hall effect. *Physical Review Letters, 71*(22), 3697–3700. https://doi.org/10.1103/PhysRevLett.71.3697

Lü, X.-L., Yang, J.-E., & Xie, H. (2025). Topological properties and resonant tunneling in graphene with

Haldane model and extrinsic Rashba effect. *iScience, 28*(9), 113354. https://doi.org/10.1016/j.isci.2025.113354

Michel, S., & Potthoff, M. (2022). Spin Berry curvature of the Haldane model. *Physical Review B, 106*(23), 235423. https://doi.org/10.1103/PhysRevB.106.235423

Nadeem, M., Hamilton, A. R., Fuhrer, M. S., & Wang, X. (2020). Quantum anomalous Hall effect in magnetic doped topological insulators and ferromagnetic spin-gapless semiconductors—A perspective review. *Small, 16*(42), 1904322. https://doi.org/10.1002/smll.201904322

Thouless, D. J., Kohmoto, M., Nightingale, M. P., & den Nijs, M. (1982). Quantized Hall conductance in a two-dimensional periodic potential. *Physical Review Letters, 49*(6), 405–408. https://doi.org/10.1103/PhysRevLett.49.405

Xiao, D., Chang, M.-C., & Niu, Q. (2010). Berry phase effects on electronic properties. *Reviews of Modern Physics, 82*(3), 1959–2007. https://doi.org/10.1103/RevModPhys.82.1959